Physica B 631 (2022) 413680

Contents lists available at ScienceDirect

Physica B: Physics of Condensed Matter

journal homepage: www.elsevier.com/locate/physb

Facile preparation of immobilised visible light active W–TiO_2/rGO composite photocatalyst by plasma electrolytic oxidation process

P. Manojkumar [a], E. Lokeshkumar [a], C. Premchand [a], A. Saikiran [a,c], L. Rama Krishna [b], N. Rameshbabu [a,*]

[a] Department of Metallurgical and Materials Engineering, National Institute of Technology, Tiruchirappalli, Tamil Nadu, 620015, India
[b] Centre for Engineered Coatings, International Advanced Research Centre for Powder Metallurgy and New Materials (ARCI), Hyderabad, 500005, India
[c] School of Marine Engineering and Technology, Indian Maritime University, Chennai, Tamil Nadu, 600119, India

ARTICLE INFO

Keywords:
Immobilised photocatalyst
Reduced graphene oxide
Plasma electrolytic oxidation
Wastewater treatment
W–TiO_2/rGO

ABSTRACT

A highly efficient immobilised W–TiO_2/rGO composite photocatalyst was prepared as a coating on titanium using plasma electrolytic oxidation (PEO) with particle addition. The high dopant concentration in TiO_2 resulted in smaller crystallite size, increased lattice strain, and dislocation density. The optimum W containing G6W sample has improved electron mobility, higher charge carrier separation efficiency, and lower electron-hole recombination rate. This can be ascribed to the number of different defect centres emerging from tungsten interstitials and higher oxygen vacancies in the TiO_2 structure. The catalyst exhibited enhanced photocatalytic degradation efficiency (93%) of methylene blue dye than the pure TiO_2, which was attributed to the synergetic effect of 2-D structured rGO and the changes incorporated upon tungsten interstitials in the TiO_2. The present research concludes that W–TiO_2/rGO photocatalyst by PEO process can be a good candidate for efficient, low cost, reusable, and visible-light-driven immobilised photocatalyst for textile wastewater treatment.

1. Introduction

Nowadays, water pollution is a significant threat to the world, and mainly the textile industry is accountable for an extensive impact and unimaginable harm to the environment [1]. Discharge of untreated dye effluents from the textile industry into the water bodies [2] contributes 80% of the total pollution caused by this industry [3]. It was estimated that around 10–50% of colouring agent released into the environment during the dyeing and finishing process [4]. Textile effluents are highly toxic, carcinogenic, and mutagenic agents and reduce light penetration, which suppresses the rate of photosynthetic activity in aquatic bodies and limits water usage downstream for irrigation, drinking, and other purposes [5]. The synthetic textile dyes are soluble inorganic compounds, making them difficult to remove from the water bodies using conventional methods [6]. Hence, an urgent need to detoxify the hazardous pollutants contaminating the water bodies by an easy, low cost, and environmentally greener approach.

Semiconductor photocatalysis (TiO_2, CdS, WO_3, ZnO) has gained potential attention in the recent past. No additional energy in the form of heat is required in this catalytic process and is considered greener to degrade the hazardous pollutants [7]. TiO_2 has been considered the most potential photocatalytic material among the semiconductor photocatalysts due to its high chemical stability, abundance, tunable microstructure, and non-toxic properties [8]. TiO_2 exists in three allotropic forms: anatase, rutile, and brookite crystal structures. An anatase structure is considered the most suitable phase for photocatalysis application, owing to its lighter effective mass and the presence of charge carriers with longer lifetimes [9]. However, its practical application is limited by several factors, such as, the TiO_2 has a high electron-hole recombination rate and wide bandgap (3.2 eV for anatase), i.e., the material will be able to absorb only UV light, which is about 4% of solar light [10]. Hence, potential research has to be made to improve TiO_2 photocatalyst by limiting the electron-hole recombination rate and tuning the bandgap of the TiO_2 semiconductor, thereby utilising the solar/visible light for photocatalytic applications.

In general, TiO_2 powder was widely used in the field of photocatalytic wastewater treatment applications. In the actual industrial wastewater treatment process, powder photocatalysts resulted in additional stages such as filtration and centrifugation to separate photocatalytic powders, resulting in the wastage of time and the incurrence of

* Corresponding author.
E-mail addresses: nrb@nitt.edu, rameshrohith@gmail.com (N. Rameshbabu).

https://doi.org/10.1016/j.physb.2022.413680
Received 27 October 2021; Received in revised form 23 December 2021; Accepted 10 January 2022
Available online 12 January 2022

the extra cost. Synthesis of an immobilised TiO_2 photocatalytic material is an effective way to overcome this problem [11,12]. Plasma electrolytic oxidation (PEO) is a novel, cost-effective electrochemical method for the preparation of manoeuvrable coatings on titanium and titanium alloys for applications in the field of photocatalysis [13–16], biomedical [17] and other industrial applications [18,19]. PEO is generally used to fabricate mono-doped, co-doped, and composite TiO_2 photocatalyst, subduing their synthesis problems by conventional methods.

Another factor that limits the effective usage of TiO_2 as a photocatalyst is the charge carrier's recombination. Various studies have been carried out in recent years to limit the electron-hole recombination by doping with metal ions (W/Mo/V/Cr/Fe/Mn/Cd, etc.) [20–23] or non-metal ions (C/N/S, etc.) [24–26] into TiO_2 matrix and forming novel composite photocatalysts by incorporating other semiconductors to TiO_2

Similarly, various approaches have been widely used to enhance the charge separation and suppress the charge carriers' recombination. Among which coupling with carbon-based functionalised materials such as CNTs, activated carbon, fullerene, graphene and reduced graphene oxide is the most promising because of their high charge carrier mobility, large surface area and mainly the superior electron trapping ability.

In recent times, reduced graphene oxide (rGO) has paid much attention to photocatalysis due to improved electron transportation and charge separation properties. Basically, rGO acts as a photogenerated electron acceptor and transporter, leading to the suppressed electron-hole recombination rate [27–29]. Reduced graphene oxides possess high specific area, strength, and excellent adsorption properties, thereby enabling them to be a more widely used material in the field of photocatalysis. Ebrahimi et al. [30] successfully developed TiO_2/rGO composite coatings on Cp-Ti using the PEO process. They found that the photoresponse of the TiO_2/rGO composite coating was superior under UV light than the pure TiO_2. The inclusion of two dimensional (2D) rGO sheets into the TiO_2 matrix paved a pathway for the electron transfer, resulting in 60% higher photoresponsive behaviour and photoswitching behaviour than the pure TiO_2.

Similarly, rGO/ZnO composite coating fabricated by the PEO process showed enhanced photodegradation efficiency due to the less electron-hole recombination rate, high specific surface area and extraordinary optical response of the incorporated rGO nanosheets [14]. TiO_2/rGO photocatalyst prepared from other techniques; for example, Sun et al. [31] designed the TiO_2/rGO composite using a single-step hydrothermal method. They found that the catalyst has increased charge separation efficiency and extended light absorption capability attributing to the excellent electrical properties of rGO and the chemical bond between rGO and TiO_2 nanoparticles. Likewise, the TiO_2/rGO photocatalyst prepared by the hydrothermal process exhibited improved photocatalytic performance. It is found that the rGO is responsible for the higher donor concentration and lower charge carrier recombination rate [32]. Similarly, Aqeel et al. [33] prepared TiO_2/rGO nanocomposite by colloidal blending process with highest photocatalytic potential, owing to the presence of rGO, which acted as adsorbent, electron acceptor, and photosensitiser in photocatalytic dye degradation.

In general, the charge carrier recombination pathway can be possible in two ways: In first, the recombination of surface electrons with holes and second, by electrons and holes within the lattice of TiO_2. It was found from the literature that the rGO coupled TiO_2 semiconductor significantly reduces the electron-hole recombination rather than activating the photoelectrons in the visible region. Also, the rGO incorporation mainly focused on suppressing charge carrier recombination on the TiO_2 surface. Hence, TiO_2 photocatalyst efficiency can be further enhanced by coupling doped TiO_2 with rGO to harvest the synergetic effect of absorption in the visible light region and reduce charge carrier recombination on both lattice and surface TiO_2 [34,35].

Wang et al. [36] prepared a composite photocatalyst comprising sulphur doped TiO_2 with rGO incorporation. The catalyst's higher photocatalytic activity was reported because the sulphur is responsible for the narrowed bandgap helping to absorb the visible light in the solar spectrum. The rGO sheets trap the electron from the CB, which rectifies the electron-hole recombination process. The synergetic effect of sulphur and rGO boost the efficiency of the S–TiO_2/rGO photocatalyst. Zhang et al. [37] developed a Co-doped TiO_2/rGO photocatalyst by hydrothermal method. The author found an optimum doping level of cobalt into the TiO_2 matrix to achieve a 99.7% degradation efficiency within a short time. This was due to the narrowed bandgap of the material about 2.92 eV and the rGO sheets in the matrix act as an electron acceptor, favouring the efficient charge separation. Similarly, Pham et al. [38] proposed a relationship between wettability and photocatalytic activity for Cu–TiO_2 and graphene oxide composite photocatalyst. The incorporation of Cu into TiO_2 lattice narrowed its bandgap. Upon irradiation, the excited electrons move from CB of TiO_2 to copper and then transfer to the graphene oxide sheets, where the electrons are trapped. As a result, recombination is delayed. Also, more hydrophilic film surface initiates higher photoreduction on MB dye.

Tungsten doped TiO_2 is widely studied and gained a potential interest in the area of photocatalysis. Tungsten is strongly known for activating the TiO_2 in the visible region and reducing the charge carrier's recombination in lattice level. To the best of the authors' knowledge, there is no study on the development of tungsten and rGO incorporated TiO_2 coating as an immobilised photocatalyst. The present research aims to develop an immobilised, visible light photoactive, and reusable rGO supported W doped TiO_2 composite photocatalyst coating on the titanium substrate by the PEO process in a single step. The present research investigated the effect of concentration of tungsten ion doping on the developed W–TiO_2/rGO composite coatings' phase composition, optical absorption, surface morphology, charge carrier's recombination rate and MB dye degradation under the visible light source.

2. Materials and methods

2.1. Fabrication of PEO coatings

The titanium substrate used in the present study is 99.90% pure. Before the PEO process, the titanium substrate is cut into the required dimensions of 20 × 15 × 2 mm. The samples were grounded, polished and ultrasonically cleaned in acetone. Custom made (Milman Thin Films Pvt. Ltd. Pune, India) pulsed DC power source unit was used for developing W–TiO_2/rGO composite photocatalyst coatings on Ti by PEO. The base electrolyte used for rGO/TiO_2 composite photocatalyst coating preparation by PEO comprises 5 g/L $Na_3(PO_4)_6.12H_2O$, 2 g/L KOH and 0.5 g/L rGO. Then Na_2WO_4 as a tungsten source was added to the base electrolyte with varying concentrations up to 8 g/L for preparing W–TiO_2/rGO composite photocatalyst coatings. The un-doped TiO_2 coating, without rGO addition, is also prepared by PEO for comparison studies. A stainless-steel pot containing electrolyte solution was used as a cathode, and the Ti substrate to be coated was immersed in the electrolyte bath acts as an anode. The Ti substrate was PEO treated for 8 min under constant current mode with a current density of 150 mA/cm^2. Also, the duty cycle and frequency were maintained at 20% and 1000 Hz, respectively. During the PEO process, the electrolyte was continuously stirred with a magnetic stirrer to ensure the homogenous circulation of the electrolyte. Additionally, the electrolyte bath temperature was controlled at 20 °C by the external refrigeration unit. After the PEO process, the coated samples were rinsed with distilled water to clean the surfaces. The sample preparation process was depicted as a flowchart shown in Supplementary Fig. S1. The identification codes for the PEO coated samples and the corresponding electrolyte composition, pH and conductivity, were presented in Table 1.

2.2. Characterisation of the PEO coated samples

The thickness of the semiconducting PEO coating was measured in

Table 1
Identification codes for the PEO treated samples along with the electrolyte composition, pH and conductivity.

Sl. No.	Sample code	Electrolyte composition	pH	Conductivity (k) (μS/cm)
1	T	5 g $Na_3PO_4.12H_2O$ + 2 g KOH	13.12	11.52
2	G	5 g $Na_3PO_4.12H_2O$ + 2 g KOH + 0.5 rGO	12.04	14.54
3	G2W	5 g $Na_3PO_4.12H_2O$ + 2 g KOH + 0.5 rGO + 2 g $Na_2WO_4.2H_2O$	11.65	15.23
4	G4W	5 g $Na_3PO_4.12H_2O$ + 2 g KOH + 0.5 rGO + 4 g $Na_2WO_4.2H_2O$	11.15	15.96
5	G6W	5 g $Na_3PO_4.12H_2O$ + 2 g KOH + 0.5 rGO + 6 g $Na_2WO_4.2H_2O$	10.62	16.35
6	G8W	5 g $Na_3PO_4.12H_2O$ + 2 g KOH + 0.5 rGO + 8 g $Na_2WO_4.2H_2O$	10.22	16.87

10 different locations using a non-destructive eddy current thickness gauge unit, and the average thickness value was reported in Table 2. The phase composition of the obtained coatings was determined by employing Ultima IV-Rigaku, X-ray diffractometer (XRD) with a Cu excitation source ($\lambda_{Cu}K_\alpha$ = 0.154 nm) over a range of 25–90° at an acquisition rate of 1°/min with the scanning step size of 0.050°. The phases present in the coatings were identified by using standard JCPDS cards. The surface morphology of the prepared coatings was investigated using a field emission scanning electron microscope (FESEM, Carl Zeiss-Gemini 300). The elemental composition was examined by x-ray spectroscopy (EDS, AMETEK-EDAX) attached to the FESEM. The surface area of the photocatalyst was measured using a BET (Brunauer-Emmett-Teller) surface analyser (Nova, Quantachrome, USA). Since the 20 × 15 × 2 mm samples are unsuitable for BET analysis, the coatings developed on 1 mm Ø titanium wire with electrolyte systems and process parameters as given in Table 1 were used for BET analysis. During the PEO process, the oxide growth occurs both outward and inward by consuming the substrate. The weight of the TiO_2 layer alone cannot be measured accurately; the total weight of the coated sample is considered in the measurement of the BET surface area. So, the surface area measured in this article for the developed photocatalyst is an apparent surface area helpful for comparing the characteristics of the fabricated photocatalysts.

Regarding the optical properties, UV–Vis diffuse reflectance spectroscopy (Shimadzu, UV-2600) was used to analyse the reflectance spectra of the coatings. The photoluminescence (PL) was measured using the spectrofluorometer (FP-8500, JASCO) with an excitation wavelength of 375 nm. The wettability of the developed coatings was analysed by measuring the contact angle of distilled water (5 μl) droplet on the coating surface using a contact angle goniometer (DSA100-KRUSS). The charge separation efficiency of the samples was analysed by the electrochemical impedance spectroscopy (EIS) using a 1 M KOH aqueous solution with a three-electrode cell setup and scanned over a frequency range of 0.1 Hz–100 kHz. The surface components of the prepared samples were observed using X-ray photoelectron spectroscopy (XPS, PHI-ULVAC) with Al-Kα (hν-1486.6 eV) as an excitation source.

Table 2
Coating thickness, phase composition and crystallite size of the PEO treated samples.

Sl. No	Sample code	Coating thickness (μ m) ±0.5 μ m	Anatase (101)		Rutile (110)	
			wt. % ±2%	D_v (nm) ±0.5 nm	wt. % ±2%	D_v (nm) ±0.5 nm
1	T	6	62	32	38	32
2	G	7	59	31	41	29
3	G2W	7.5	91	28	09	26
4	G4W	9.5	100	26	00	–
5	G6W	11	100	25	00	–
6	G8W	11.5	100	24	00	–

The photocatalytic ability of the prepared samples was evaluated by the degradation of MB under visible light irradiation. The prepared photocatalyst of dimension 15 × 10 mm, like three samples, was immersed in the 15 ml of 20 mg/L aqueous MB solution at room temperature. MB solution was maintained in a dark condition before initiating the photocatalytic process to achieve the adsorption-desorption equilibrium. In order to find the adsorption capability of the photocatalyst, the prepared samples were immersed in the MB solution and kept in the dark condition for about 60 min. The absorption spectra of the resultant MB solution were analysed in UV–Vis spectroscopy. Photocatalysis was carried out by irradiating the samples, dipped in MB solution, using a 300 W tungsten lamp was used as the light source. The irradiation source was set at 15 cm above the MB solution. The light ————intensity was measured by a CMP3 pyranometer, and the value is 60 ± 5 mW/cm^2. Blank experiments were conducted on MB solution without any samples to analyse its direct photocatalytic nature, which shows the MB solution was stable even after 3 h of visible light irradiation. The degradation rate of the MB was analysed by taking a 2 ml of MB solution for every 30 min to measure the absorption spectra relative to the concentration of MB in the aqueous solution and then replenished back after the measurement to maintain the uniform volume of the solution throughout the process. To evaluate the recyclability of the best photocatalyst sample, the used photocatalyst was retrieved and underwent dye desorption by freshwater cleaning and ultrasonication with water and ethanol for 15 min each.

3. Results and discussion

3.1. Phase analysis of the samples

The crystal structure of the as-prepared samples was characterised by the powder X-ray diffraction (XRD) technique. The XRD patterns of the substrate (S), TiO_2, TiO_2/rGO and tungsten doped TiO_2/rGO composite coated samples are shown in Fig. 1. The peaks at diffraction angles (2θ) of ~25.3° and ~27.4° (JCPDS card no. 21–1272 and 21–1276) in the XRD pattern of the coated samples represent the principal crystal planes of anatase and rutile TiO_2 phases, respectively. Additionally, there is no evidence of carbon-related peaks in the samples incorporated with rGO. Also, it can be believed that the rGO peak might be overlapped with the characteristic peak of the anatase TiO_2 [39]. The wt. % of anatase and rutile phases of TiO_2 in the prepared samples was calculated using the Spur formula, and the values are reported in Table 2. The samples T and

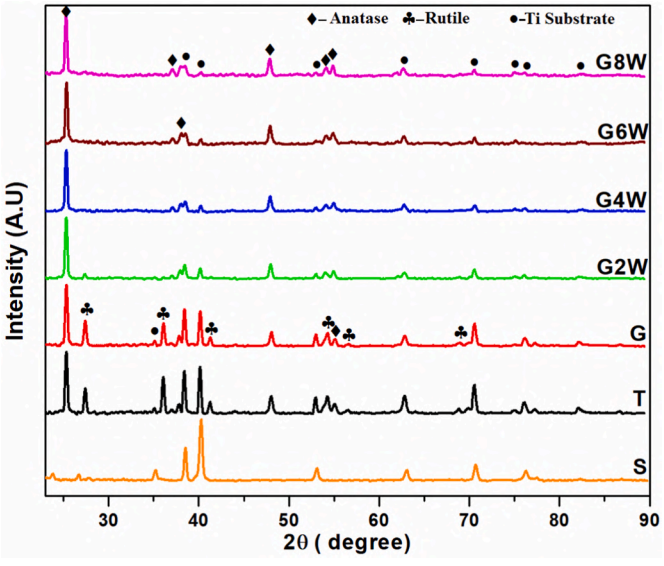

Fig. 1. XRD analysis of the PEO samples and uncoated substrate.

G show both anatase and rutile phases of TiO_2. It was implied that incorporating rGO does not alter the structural property of sample G. In contrast, the G2W sample has a considerably lower intense rutile peak than the undoped sample. It was suggested that tungsten dopant concentrates on the surface of the TiO_2 grains and hinders the crystal growth, thereby retard the anatase to rutile phase transformation. Corroborating with G2W, the samples doped with a higher concentration of tungsten, namely G4W, G6W and G8W, shows the zero-rutile content indicating complete suppression of anatase to rutile transformation. This is because the doped W^{6+} ion diffuses into the interstitial positions of the TiO_2 lattice, thereby decreasing the density of oxygen vacancies which results in retardation of the anatase to rutile phase transformation [40]. The average crystallite size (D_v) of the TiO_2 phases was assessed using the Debye-Scherrer equation and presented in Table 2. It was found that the crystallite size of the prepared samples decreased with the increase of tungsten concentration into the TiO_2 lattice. This may be due to a slight distortion in the crystal lattice upon doping with metal ions [41]. The ionic radii of W^{6+} (0.600 Å) and Ti^{4+} (0.605 Å) are almost similar, with no significant change in the TiO_2 unit cell on substitutional doping. In contrast, partial replacement of Ti ion with W^{4+} (0.66 Å) imparts minor expansion in the TiO_2 unit cell. The lattice parameters of the unit cell of the prepared samples have been calculated by fitting the XRD data using GSAS II software. Also, the lattice strain (ε), dislocation densities (δ) and theoretical specific surface area (S_a) were calculated by the procedure mentioned in Ref. [42], and the values are reported in Table 3. The sample G with little change in the lattice strain and dislocation density indicates no changes resulting from the interaction of TiO_2 and rGO sheets. Due to the Ti and dopant ionic radii mismatch, a minor strain is induced in the TiO_2 crystal lattice. The increase in lattice strain and dislocation density implies that the doped samples have more defects in the crystal lattice. This can extend light absorption in the visible light spectrum. It also favours decreasing the charge carriers recombination rate and increasing the separation of the photo-induced electrons and holes [43]. The limited solubility of W^{6+} in the TiO_2 lattice leads to limited expansion in the unit cell volume, whereas the effect of stress still exists with the tungsten doping. Hence, the cell volume with lattice strain and dislocation density increases with further tungsten concentration. The other factor responsible for the degradation of methylene blue is the adsorption of MB dye onto the surface of the TiO_2 photocatalyst, which is highly dependent on the surface area. The specific surface area of the doped samples was increased with the increase of dopant concentration. As a result, the higher specific surface area can increase the contact area with dye solution and provide more active sites for the adsorption of dye molecules, increase the productivity of generated electron-hole pairs, and promote photocatalytic activity.

3.2. Surface morphology of the developed coatings

The surface morphology of the developed PEO and PEO coatings, along with EDS spectra, are shown in Fig. 2. All the samples exhibit porous surface morphology, and the dopant's addition significantly influenced the sample surface. The sample G exhibited a large cluster of pores with irregular shapes. The sample G2W with the least concentration of W among the coatings shows partial removal of large clusters. In contrast, the sample G4W reveals the surface is entirely free from the large clusters and develops into more perfect uniformly distributed toroidal structures similar to the result found in the study [44]. Since the rGO sheets were highly inert and stable, a negative charge is established in the rGO as soon as it enters the alkaline electrolyte. The rGO sheets were migrated near to the pores of the positively charged anode by virtue of electrophoretic force [40]. Fig. 2 also shows the high-magnification FESEM micrographs with the successful incorporation of rGO sheets in the developed coatings. The samples G and G2W exhibit the rGO sheets embedded partially near the pores, whereas G4W, G6W and G8W indicate rGO sheets were entrapped within the pores. Since the conductivity of the electrolyte used in the preparation of coatings increases with the increase of W concentration, the discharge characteristics and thermal reactions that occur at discharge sites alter the PEO process and thereby resulted in obtaining different surface morphologies. During the PEO process, the rGO nanosheets entrap in the vicinity of the discharge channel and accordingly, the number of pores is reduced [45].

Fig. 3 shows the porosity map of the samples derived from the FESEM images using ImageJ software. The sample T and G show uneven pores with 7.5 and 6.5% porosity, respectively. The sample G2W shows the porosity of 23.6%, whereas the samples G4W, G6W and G8W show porosity of 22.5%, 21.8%, and 21.2%, respectively. The secondary electron (SE) image and the corresponding backscattered electron (BSE) image, and EDS maps of sample G6W were shown in Fig. 4. The BSE image shows that the carbon-based rGO with the least atomic number was dark. In contrast, titanium and other elements with a higher atomic number appear bright in the BSE image. The EDS mapping shows the presence of individual elements, which constitutes the surface of the coating. The presence of tungsten is confirmed by the EDS analysis with the W Mα peak at 1.77 KeV. It is evident from the EDS spectra that the intensity of the W Mα peak increases with the increase of W dosage in the electrolyte. Table 4 depicts the EDS elemental composition present in the prepared samples. From Table 4, it is evident that the at. % of W was found to be increased with the increase in W concentration in the electrolyte. The carbon content related to the rGO varied only slightly in samples with varied W concentrations. The nitrogen adsorption-desorption isotherm of the prepared samples was shown in Fig. 5 to understand the specific surface area. All the photocatalysts, except sample T, show high nitrogen adsorption-desorption isotherms due to the higher surface porosity, thereby providing more active sites for photocatalytic reactions. The surface area of the samples T, G, G2W, G4W, G6W and G8W are 2.43, 4.45, 4.85, 5.15, 7.23, 7.85 m^2/g, respectively.

Table 3
Structural parameters, lattice strain, dislocation density and specific surface area of the PEO treated samples.

Sample Code	Lattice parameters		Unit cell Volume. Å^3	Lattice Strain (ε) 10^{-3}	Dislocation density (δ) Lines/nm^2	Specific surface area (S_a) x 10^5 cm^2/g
	a/Å	c/Å				
T	3.7419	9.4598	132.930	1.082	0.000976	4.6957
G	3.7482	9.5012	133.482	1.130	0.001040	4.8715
G2W	3.7518	9.5767	134.877	1.258	0.001275	5.4497
G4W	3.7548	9.6035	135.395	1.332	0.001479	5.8914
G6W	3.7556	9.6134	135.622	1.386	0.001600	6.1365
G8W	3.7576	9.6169	135.835	1.402	0.001736	6.4036

3.3. Wettability of the coatings

The contact angle (CA) of the prepared coatings was measured between the water droplet and the surface of the coated samples, as shown in Fig. 6. The bare TiO_2 shows a contact angle of $59^\circ \pm 2$. In contrast, the sample G with rGO displays a relatively higher contact angle value of $65^\circ \pm 2$, which can be associated with the presence of wrinkled or folds of rGO layer, which entraps the air bubbles, drastically reducing the contact area of the water droplet on the surface of the coatings. On the other hand, the CA value of W doped TiO_2/rGO composite coatings was found to vary from $76^\circ \pm 2$–$85^\circ \pm 2$ with the increase of W concentration (2 g/L to 8 g/L) in the electrolyte, which can be ascribed to the nano protrusions associated with the nanopores as well as 2-D structured rGO layer [46]. All the developed coatings show the hydrophilic nature, facilitating the easy spreading of wastewater and adequately improving photocatalytic reaction rate.

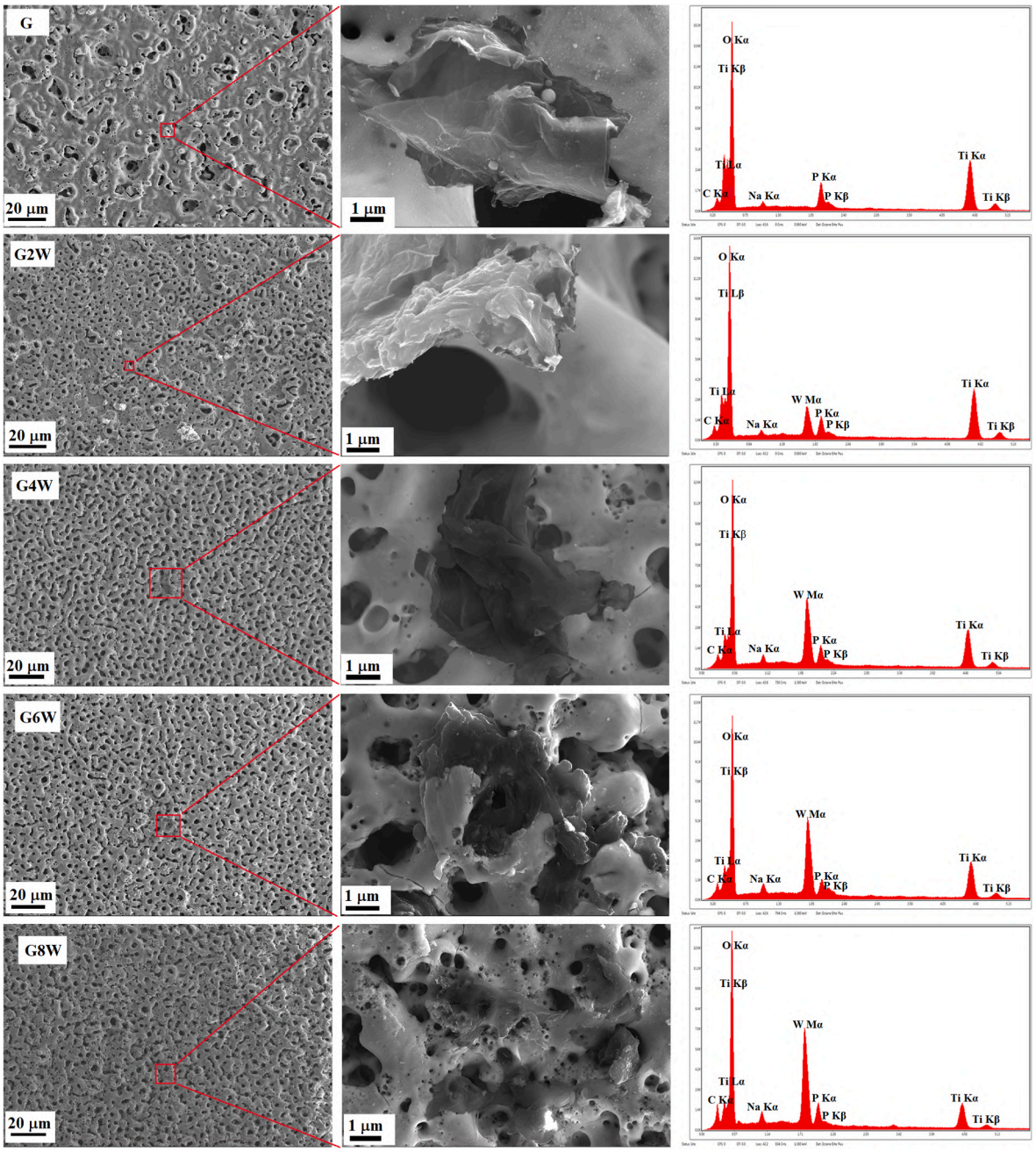

Fig. 2. Surface morphology and EDS analysis of the PEO samples.

3.4. Optical properties of the coatings

The absorption edge of the samples TiO_2, G and W doped TiO_2/rGO was acquired from the UV–Vis DRS absorbance spectra derived from the corresponding UV–Vis DRS reflectance spectra using the Kubelka-Munk function, and it is presented in Fig. 7a. The absorption edge of the bare TiO_2 is in the UV regime, whereas the sample G with rGO sheets exhibits an absorption edge in the near-visible region. The slight shift in the absorption edge towards the visible region can be attributed to the incorporation of high specific surface area 2-D structured rGO into the TiO_2 layer, furthermore, the formation of Ti–C chemical bond between the TiO_2 and rGO, which account for the contraction of the bandgap in the TiO_2/rGO composite [47]. This will enhance the light absorption ability of the TiO_2/rGO composite, which is not sufficient to excite the electron from the conduction band to the valence band with lower light energy. The UV absorption edge of the W doped TiO_2/rGO composite shows a tremendous shift towards the visible region. This might be attributed to the formation of donor level under the conduction band of TiO_2, leading to a narrower bandgap. The sample G8W reveals the absorption edge almost identical to the G6W, which confesses that increasing W concentration above 6 g/L does not improve further. The optical bandgap of the indirect band TiO_2 semiconductor was measured using the variation of the absorption coefficient $(\alpha h\nu)^2$ of the coatings with photon energy ($h\nu$) as stated in the Tauc relationship [20]. The extrapolation of the linear region of curves determines the bandgap of the samples. The Tauc plots of the prepared samples are shown in Fig. 7b. The bandgap of the samples T, G, G2W, G4W, G6W and G8W are 3.13 eV, 3.09 eV, 3.02 eV, 2.92 eV, 2.88 eV and 2.89 eV, respectively. The narrowed bandgap can be ascribed to the increase in the lattice defects as a result of W doping and rGO addition, which creates a localised W 5d state just below the conduction band (CB) minimum and manoeuvre the conduction band to a lower level, which results in the

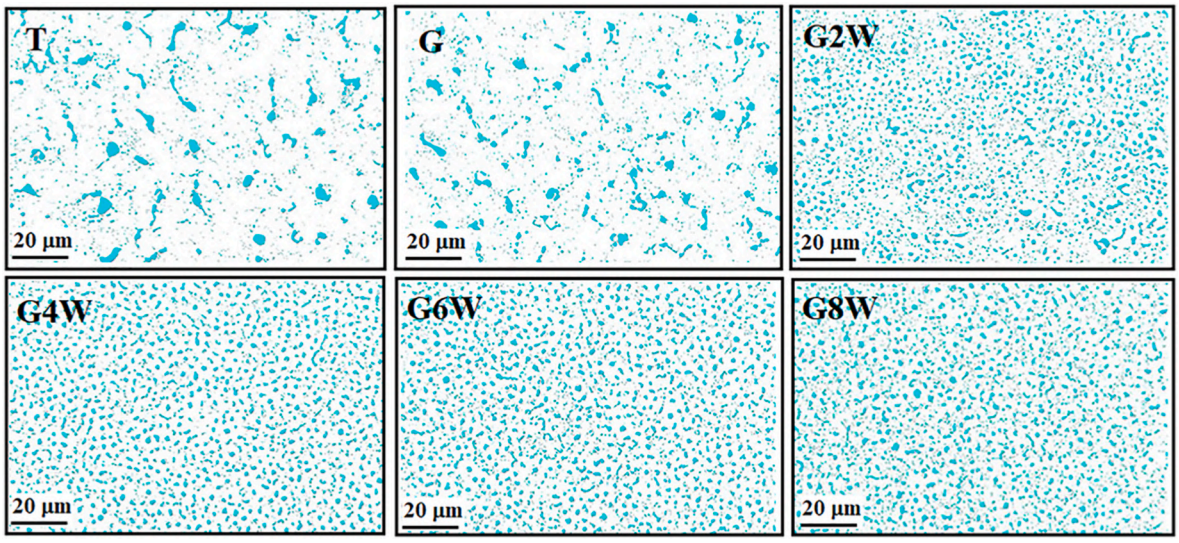

Fig. 3. Porosity map of the PEO coatings.

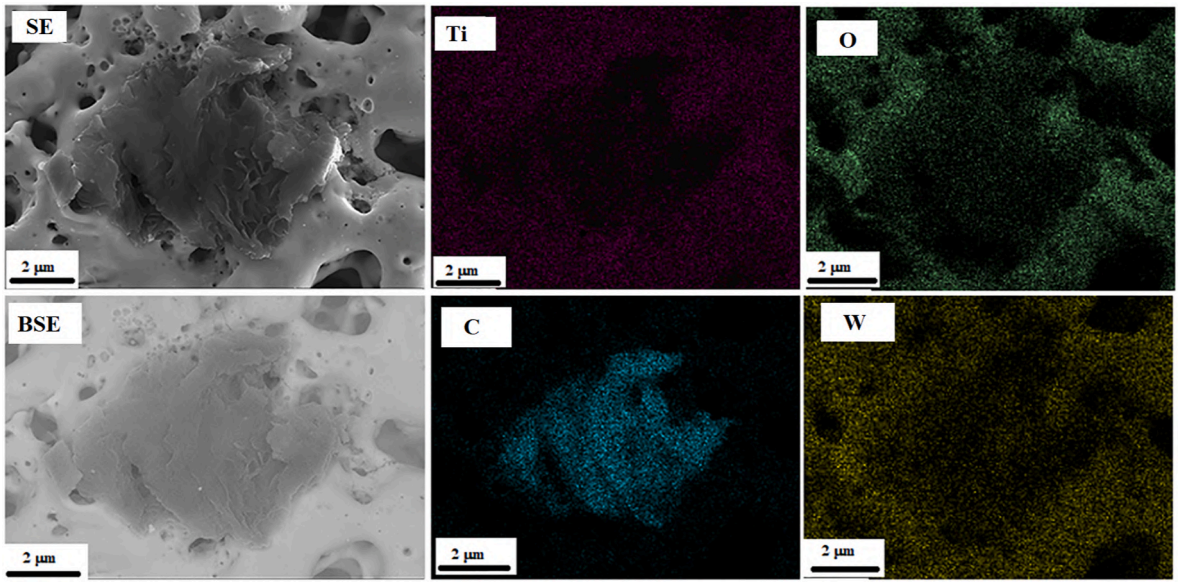

Fig. 4. The SE image, corresponding BSE image, and EDS elemental maps of sample G6W.

Table 4
EDS surface composition of the PEO treated samples.

Sample code	Element (at. %)					
	O	Na	P	Ti	C	W
T	65.40	0.90	4.7	29	–	–
G	62.12	0.81	4.81	27.62	4.64	–
G2W	62.95	0.75	3.49	26.88	4.55	1.38
G4W	64.61	0.80	2.47	24.49	4.43	3.20
G6W	63.86	0.74	2.96	23.52	4.27	4.65
G8W	63.27	0.85	2.43	23.39	4.12	5.94

contraction of conduction band to valence band energy [48]. All the W–TiO_2/rGO composite samples exhibited a lower bandgap value suitable for the visible light photocatalytic process.

3.5. Photoluminescence emission spectrum from the coatings

PL emission spectra are useful for measuring the photon emission and its energy distribution upon optical excitation and providing insight into the electron-hole recombination rate in photocatalytic materials. Also, the lattice distortion and oxygen inadequacy present in the prepared samples were analysed using PL emission spectra presented in Fig. 8. The PL spectra were recorded over 380 nm–525 nm with an excitation wavelength of 375 nm at room temperature. All the samples show the PL emission spectrum with a similar peak pattern, but the intensity of the emissions is remarkably different. The PL emission spectra constitute many peaks in which the main emission band located at 400 nm corresponding to the band-to-band transition of TiO_2, and various peaks ranging from 450 nm to 480 nm originated from the charge transfer transition of an oxygen vacancy and other defects including rGO sheets [43,44]. Compared to samples T and G, the samples G2W, G4W, G6W, G8W show a minor redshift in the 400 nm band to band emission peak. This redshift can be attributed to the reduction in the bandgap of the TiO_2 by the evolution of the density of states tails band from inhomogeneous distribution of dopants, which is consistent with the UV–Vis absorption spectra in Fig. 7. The PL emission spectra constitute many peaks in which the main emission band is located at

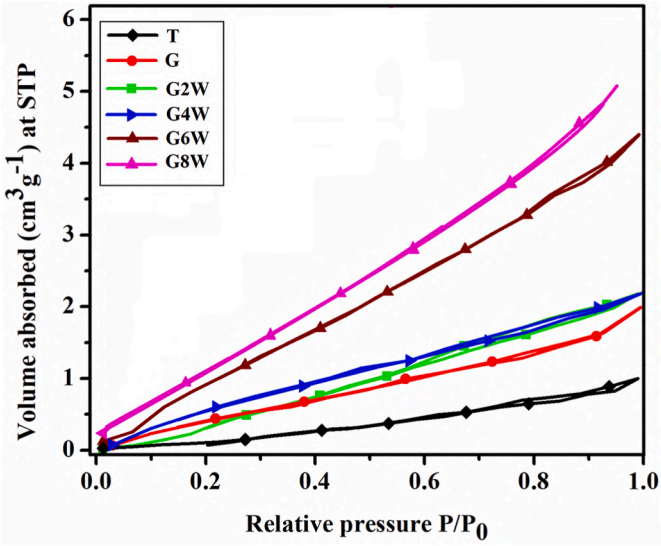

Fig. 5. Nitrogen adsorption-desorption isotherm for the PEO samples.

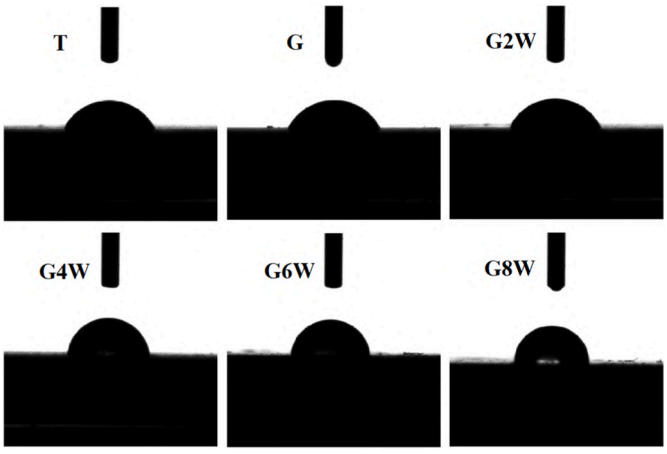

Fig. 6. Water droplet images indicating wettability of the PEO coatings.

400 nm corresponding to the band-to-band transition of TiO_2 and various peaks ranging from 450 nm to 480 nm. The peaks located ~450 nm and ~468 nm are arising from oxygen vacancies trapping the electrons. These charge carriers are generally trapped by surface hydroxyl groups and oxygen vacancies that contribute to their visible luminescence [49]. The charge transfer transition from Ti^{3+} to oxygen anion gives emission peaks at ~483 nm and ~494 nm [50–52]. The sample T shows the PL emission with elevated intensity resulting from the fastest recombination of charge carriers, which can be attributed to the lack of defects in the crystal to trap the charge carriers. Also, surface recombination occurs in the absence of rGO. On the other hand, the sample G with rGO content exhibits relatively lower intensity PL spectra than sample T, resulting from the unique 2-D structured rGO in the TiO_2 layer [30]. The excited electrons from the CB of TiO_2 were transmitted into the rGO sheets, diminishing the charge carriers' recombination rate. The samples with TiO_2/rGO with W dopant show a reduction in PL emission intensity with the increase of W dosage. The lowest intensity was recorded on the sample G6W, indicating the suppressed recombination rate of photoexcited charge carriers resulting from the synergetic effect of surface electron trapping by 2-D structured rGO and the tungsten as electron acceptor also the formation of different defect centres emerging from oxygen vacancies in the TiO_2 [48–53]. The PL intensity of the sample G8W is relatively higher than the sample G4W and G6W, which can be attributed to the excess W dopant in the TiO_2 [54]. This depicts that the optimum level of doping is crucial for lowering the electron-hole recombination rate. Otherwise, the surplus doping act as recombination centres; thereby, the photocatalytic activity of the sample can be significantly decreased.

3.6. EIS and photocurrent analysis of the prepared coatings

Interface charge carrier transfer and separation efficiency are some of the prominent factors that affect the photocatalytic ability of the prepared samples. Hence, electrochemical impedance spectroscopy (EIS) was used to ascertain the resistance offered by the sample for efficient charge separation of photogenerated electrons and holes. Fig. 9 shows the Nyquist plot of EIS for the prepared samples under dark and visible light irradiation conditions. The arc radius of the Nyquist plot suggests the rate of the reaction on the photocatalyst. A greater arc radius represents a substantial amount of resistance the material offers for charge transfer [55]. The Nyquist plot of samples shows similar semicircles with different radius. The radius was significantly reduced under illumination than the dark condition, which confesses that the sample is prominently active under the visible light illumination. The

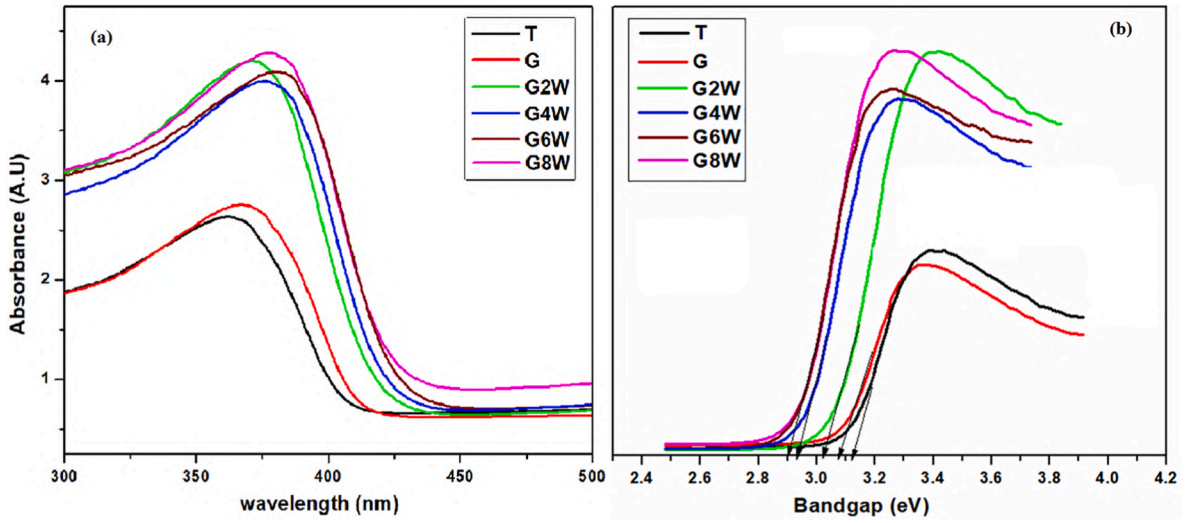

Fig. 7. UV DRS absorbance and Tauc-plot for the PEO coatings.

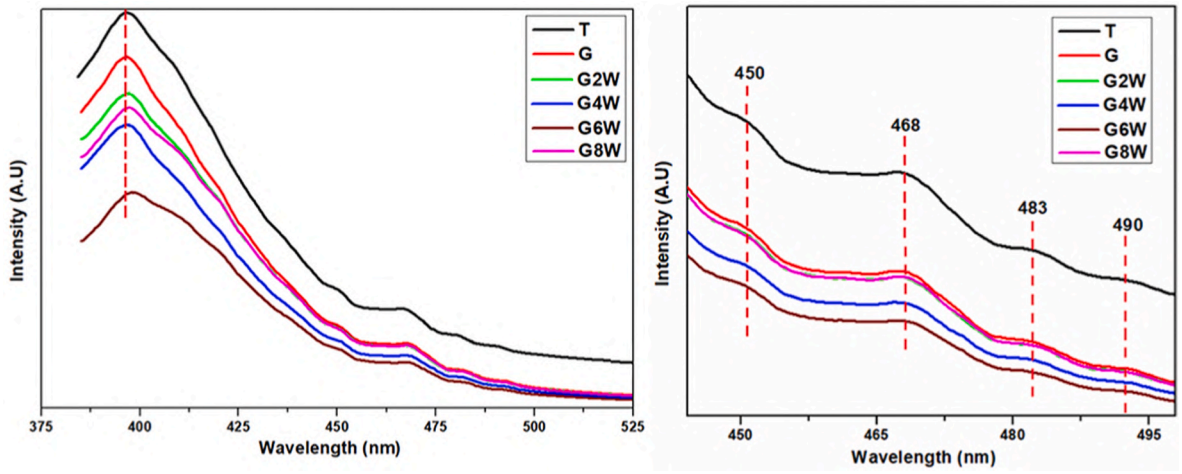

Fig. 8. PL emission spectra of the PEO coatings.

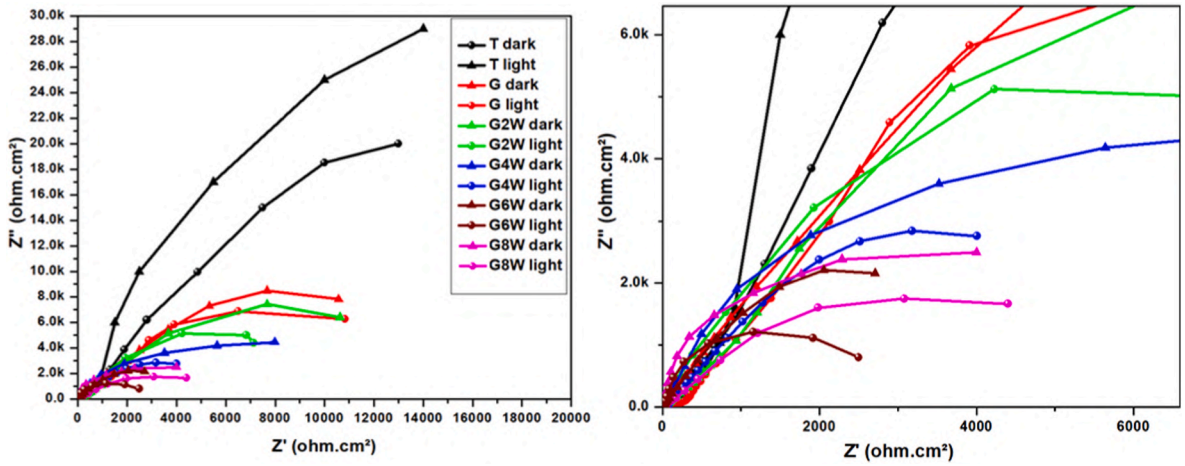

Fig. 9. EIS-Nyquist plot of the PEO samples.

smallest semicircle was reported for the sample G6W in both dark and visible light irradiation, indicating that its resistance to the interfacial charge carrier transfer was weakened, i.e., high charge separation efficiency. These results clearly show that the synergetic effect of optimal dosage W and 2-D layer rGO sheets could effectively facilitate the electron-hole mobility and improve the charge carrier separation efficiency in the W doped TiO_2/rGO composite [20,30]. It was apparent from the UV-DRS, PL spectra, and EIS measurements that an optimum doping amount of tungsten is crucial in TiO_2 photocatalyst to mitigate the recombination of photogenerated electron-hole pairs. The Nyquist plot gave a piece of solid evidence to support the above discussed UV-DRS & PL results. Thus W–TiO_2/rGO composite can be used as an effective material for photocatalytic application. The photocurrent was evaluated by measuring the photocurrent density at varying potential with the range of −1.5 to 2.5 V vs SCE with the sweeping rate of 60 mV/s in 0.1 M Na_2SO_4 medium. The linear sweep voltammetry (LSV) graph of prepared photocatalyst under dark and visible light irradiations are shown in Fig. 10. The photocurrent density of all the samples under dark medium shows only a narrow photocurrent value, compared to the visible light irradiation. This indicates that the prepared catalyst responds to the irradiation of visible light and produces a photocurrent. The photocurrent density of photocatalyst under illumination is gradually increased after incorporating rGO and with increasing concentrations of W dopant. It confirms that W doping and rGO incorporation are effective and straightforward methods for enhancing photocatalytic

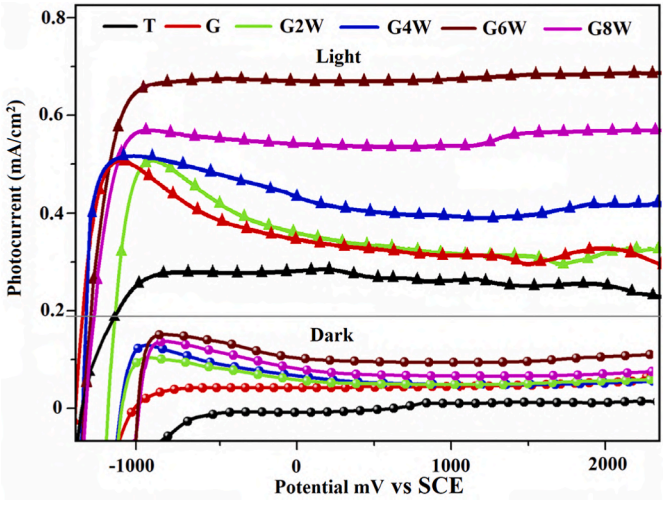

Fig. 10. Photocurrent density of the PEO coatings collected at dark and light conditions.

degradation performance. Also, the photocurrent density increases gradually with the applied potential and reaches a saturated current of 0.68 mA/cm^2 at −1 V vs SCE. By analysing the above photocurrent

graph, it has been found that the photocurrent densities of the G6W sample are almost two times higher than that of pure TiO_2 (sample T) in the entire scan range. The higher photocurrent density of the G6W sample is ascribed to the narrowed bandgap indicating the efficient absorption of the light energy from the visible spectrum. This higher photocurrent implies a higher photocatalytic degradation efficiency for the sample G6W.

3.7. X-ray Photoelectron Spectra of the prepared samples

X-ray Photoelectron Spectra (XPS) provides surface-sensitive information about changes in the chemical state of elements present in the composite coating. The XPS peaks were deconvoluted using curve fitting software (Gaussian deconvolution) CASAXPS. Fig. 11 shows the survey spectrum and high-resolution XPS spectra of Ti 2p, O 1s, C 1s and W 4f for the samples T, G and G6W. The survey spectrum confirms the presence of TiO_2, W and C species in the photocatalyst. The Ti 2p core level of the sample T and G shows doublet peaks at the binding energy of 457.4 eV and 463.4 eV, matching Ti 2p3/2 and Ti 2p1/2, respectively a valence state of Ti^{4+} of TiO_2 [30]. The incorporation of rGO does not alter the peak position of the Ti^{4+} since rGO sheets mainly exist on the surface of the TiO_2 and do not modify the crystal structure of the TiO_2. On the other hand, the sample G6W shows a slight shift of 0.5 eV in the position of the doublet peak as 457.9 eV and 463.9 eV, which can be ascribed to the substitutional doping of W into TiO_2 lattice, which produce a slight distortion in the crystal lattice upon doping with tungsten ions. All the samples show a small shoulder peak at a binding energy of 459 eV associated with the $Ti^{3+}$of Ti_2O_3. The sample T without adding any dopant and rGO also shows Ti^{3+}, which can be attributed to the inevitable doping of phosphorous present in the base electrolyte used to prepare coatings [20]. In sample G6W, the Ti^{3+} peak shows a higher area fraction compared to that in the samples T and G. The increase in the intensity of the Ti^{3+} peaks ascribed to the charge compensation by electrons corresponding to substitutional doping of W^{6+}/W^{4+} species for Ti^{4+}, which will lead to the reduction of titanium oxidation state, i.e., Ti^{3+} [56]. The presence of Ti^{3+}results in the generation of more oxygen vacancies to maintain the local neutrality in the TiO_2 lattice [57]. Additionally, Ti^{3+} can also suppress the charge carrier recombination rate and promote charge separation efficiency [58].

The high resolution (HR) -XPS scan of O 1s core level for samples T, G, and G6W was deconvoluted into two peaks at a binding energy of 529.8 eV and 531.6 eV. The first peak of O 1s spectra belongs to the lattice oxygen of the Ti–O bond (TiO_2), whereas the second peak corresponding to the non-lattice oxygen of O–H belonging to the adsorbed species (superoxide, water molecule or hydroxyl group) [57]. The peak corresponding to non-lattice oxygen of sample G6W shows an increase in intensity, confirming the substitutional doping of tungsten at TiO_2 lattice. The suppression in the recombination rate of charge carriers might be due to the reaction of photogenerated holes with the adsorbed species (i.e., superoxides etc.) present in higher amounts on the surface, thereby enhancing the charge transferability of the photocatalyst. Consequently, the production of strong hydroxyl groups can lead to the degradation of organic compounds in textile dyes.

The HR-XPS scan of C 1s core level for samples G and G6W was deconvoluted into five peaks at binding energy 284.3, 285.2, 286.5, 287.4 and 289.2 eV corresponding to Ti–C, C–C, C–O, C═O and O═C–O functional groups, respectively [59]. The peak related to Ti–C is attributed to the chemical bonding between titanium and carbon from the rGO, which confirms the interaction between TiO_2 and rGO sheet through the rearrangement of Ti atoms [57]. The TiC peak in sample G6W shows lower intensity than in sample G, which can be ascribed to the interaction of TiO_2, and W is more influential than the TiO_2 and rGO. The XPS spectra of the W 4f core level were deconvoluted into different peaks. In which the peaks located at 34.8 and 36.6 eV corresponding to $4f_{7/2}$ and $4f_{5/2}$of W^{6+}. Consequently, a small doublet peak positioned at 32.4 and 34.2 eV corresponding to $4f_{7/2}$ of W^{4+} [60,61]. The W 4f core level confirms the tungsten species may be present in TiO_2 with different oxidation states.

3.8. Photocatalytic activity of W doped TiO_2/rGO composite coatings

Fig. 12 represents the UV–Vis absorption spectra of the MB solution degraded under a visible light source over an irradiation period of 180 min. The UV–Vis absorption spectra were measured over a range of 200 nm–800 nm. All the samples show the spectra with the same pattern but with different intensity. Additionally, to evaluate the adsorption ability of the photocatalyst, experiments were conducted in the dark medium before the degradation of MB dye under visible light. From Fig. 13a, it can be concluded that the entire W doped TiO_2/rGO composite poses notable adsorption ability, precisely; sample G4W, G6W and G8W shows

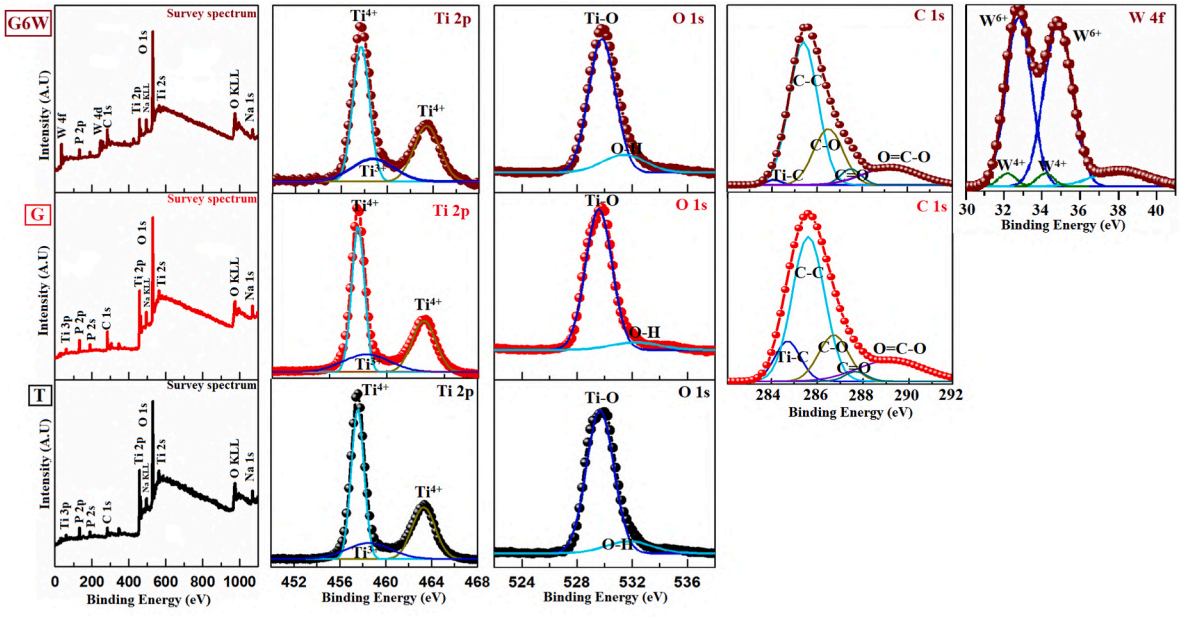

Fig. 11. XPS survey spectra of T, G and G6W photocatalyst and the corresponding high-resolution XPS spectra.

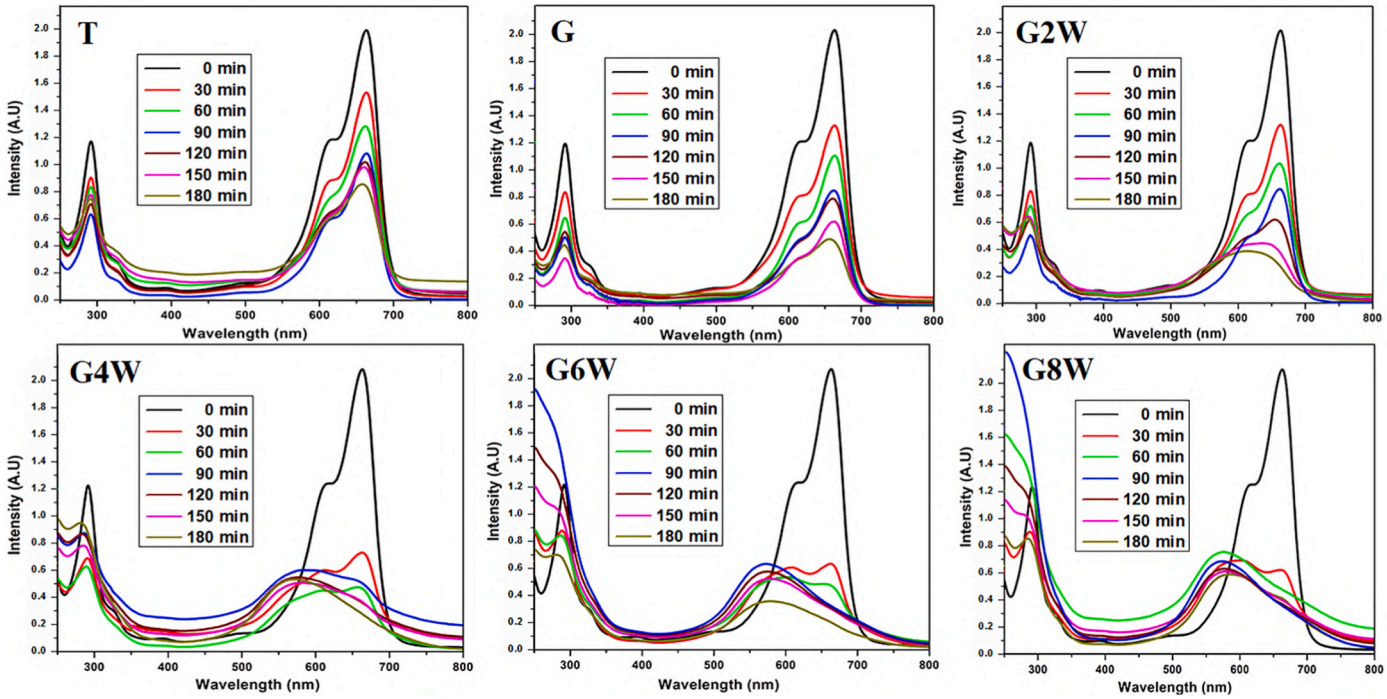

Fig. 12. UV–Vis absorption spectra of MB dye degradation by various PEO samples.

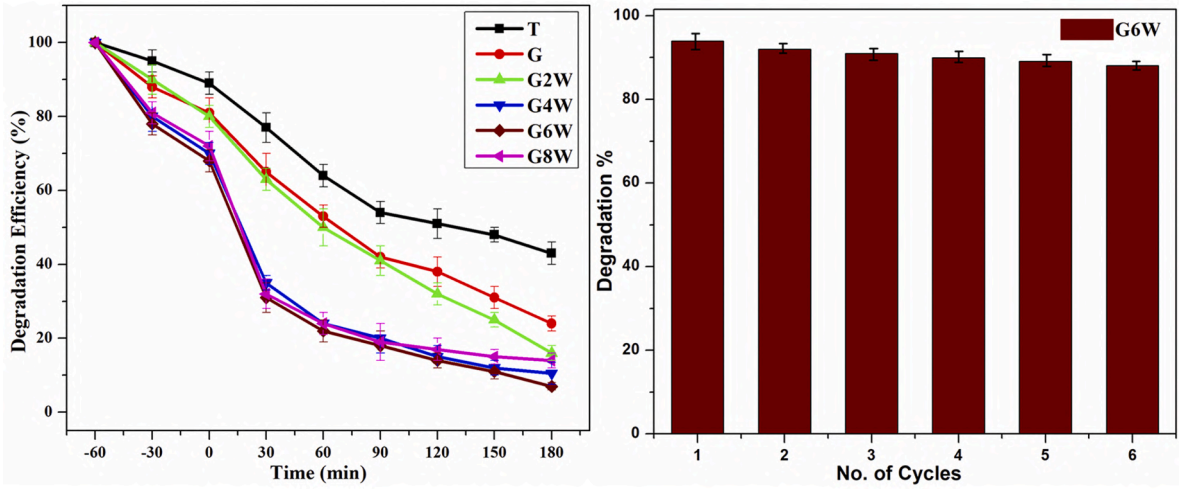

Fig. 13. (a) Photocatalytic degradation of MB dye for the PEO treated samples and (b) reusability of G6W sample.

a maximum adsorption efficiency of 28, 33 and 31%, respectively. This might be ascribed to the presence of porous morphology with uniformly distributed pores and the surface energy of the photocatalyst. Also, the photosensitisation properties and strong electrostatic attraction of cationic molecules of MB dye towards the sample plays a vital role in the adsorption properties [62,63]. Sample T reports the MB degradation efficiency of 43%, which is much lower than the sample G with 72% degradation efficiency. The increase in efficiency could be attributed to the presence of unique 2-D structured rGO sheets in the TiO_2 layer, which is responsible for the trapping of electrons excited from the CB and leads to a longer charge carrier's life. The improved shelf life of the electrons and holes can result in the interaction with the water molecules and oxygen to create more hydroxide radicals and superoxide anions, which attack the dye molecules, thereby degrading the MB dye more effectively [64]. The sample TiO_2/rGO with varied W concentration (2 g/L to 8 g/L) shows tremendous improvement in the MB dye degradation efficiency. Additionally, a blue shift in the UV–Vis spectra was also recorded for the samples G4W, G6W and G8W. The maximum absorbance peak of MB dye was recorded at 664 nm for the initial condition, and as time progresses, its intensity gradually decreases along with the peak shift towards a lower wavelength. This can be ascribed to the destruction of the parent compound and the formation of new intermediate compounds [65,66]. The sample G6W shows the highest degradation among all the prepared samples, which account for 93% efficiency. The sample G8W with a higher concentration of tungsten 8 g/L shows 88% degradation efficiency. The sample G2W with a lower concentration of tungsten results in 76% degradation efficiency, the least among the tungsten doped TiO_2/rGO samples. This might be ascribed to the lower dosage of tungsten, thereby forming relatively fewer defect centres and faster charge recombination. The present photocatalyst showed better degradation efficiency (with respect to catalyst dosage, dye concentration, light source and degradation time)

compared to most photocatalysts prepared by other processes [20, 30–33,67–70]. This proves that the present W–TiO_2/rGO photocatalyst can effectively degrade bulk MB dye concentration. The photocatalyst stability was investigated by conducting the degradation test for almost 6 cycles for optimum W doped sample G6W, as shown in Fig. 13b. This reusability test reveals that all the cycles' efficiency values were reported to be satisfactory.

The overall improvement in the development of optimised W–TiO_2/rGO composite coating for the effective degradation of MB dye results from the synergetic of 2-D structured rGO and the formation of different defect centres emerging oxygen vacancies on the TiO_2 along with narrower band gap, porous surface morphology with expected high surface area, improved electron mobility with efficient charge carrier separation and lower recombination rate.

3.9. Proposed mechanism for the degradation of MB dye using W–TiO_2/rGO photocatalyst

To understand the mechanism of photocatalytic degradation, the trapping experiment was carried out by using different kinds of scavengers such as q-benzoquinone reagent (BZQ, as a superoxide scavenger), ethylene diamine tetraacetic acid disodium (EDTA-2Na, as a hole scavenger and isopropanol (IPA, as a hydroxyl radical scavenger), were added into the MB dye solution. The scavenger concentrations were set at 1 mmol for the trapping experiment, and the results are shown in Fig. 14. The IPA and EDTA-2Na added MB solution degradation was severely affected and reduced to 45% and 48%, respectively. Whereas the BZQ added MB solution was 75% degradation, which confesses the superoxide scavenger has a limited effect on the MB degradation process. Finally, it was concluded that the hydroxyl radical and holes were the active species responsible for the degradation of MB dye.

Based on the active species test in the present work and reported literature, the photocatalytic degradation mechanism of MB dye solution by the W–TiO_2/rGO photocatalyst under visible light irradiation was proposed in Fig. 15. The MB degradation process was assumed to involve the following three steps. Step 1: Adsorption of MB dye by the prepared W doped TiO_2/rGO photocatalyst. Step 2: Activation of photocatalyst by absorbing the visible light. Step 3: Generation of active radical species by the charge carriers to degrade the MB dye into CO_2 and H_2O. When the W–TiO_2/rGO photocatalyst is kept under the MB dye solution, adsorption of MB dye towards the catalyst is started. The hydrogen bonding achieved the excellent adsorption capability of the developed photocatalyst, π–π coupling between the aromatic region on

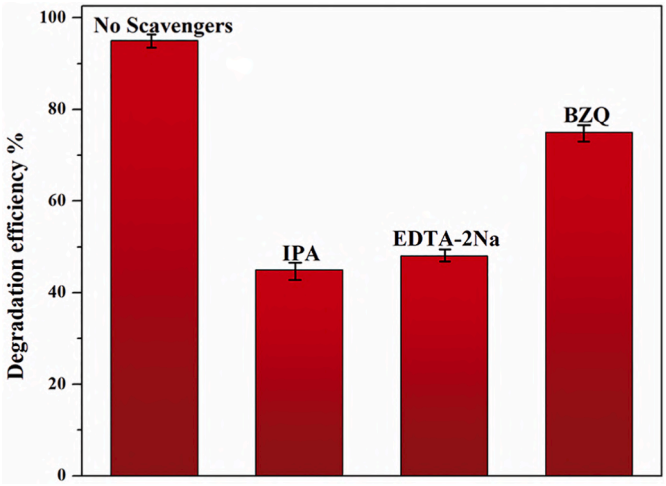

Fig. 14. Radicals scavenger test over G6W in the MB photodegradation process.

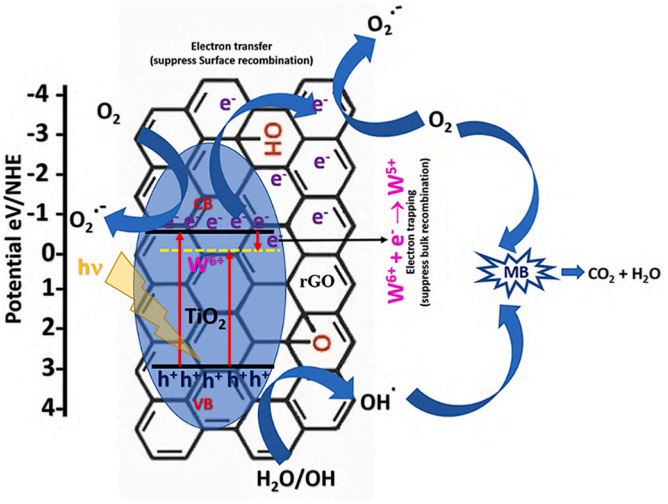

Fig. 15. Schematic illustration of the photocatalytic degradation mechanism of MB dye onto G6W photocatalyst.

graphene's surface and aromatic molecules strengthens the interaction with rGO-MB electrostatic interaction between the photocatalyst and MB dye. This adsorption process dramatically improves the photodegradation process by accumulating the abundant MB dye near the photocatalyst.

Under visible irradiation, the W–TiO_2/rGO photocatalyst gets activated and excite the photoelectron to the CB of TiO_2, leaving behind the holes in the VB of TiO_2. Whereas the W dopant in the form of W^{6+} forms a shallow energy level near the conduction band minima (CBM), which acts as the trapping site, and the electron can be accepted by W^{6+} to form W^{5+} . Which in turn improve the lifetime of electrons and holes also reduce the recombination of charge carriers. Therefore, the coexistence of W^{6+}/W^{5+} couples, charge carriers, and surface oxygen species such as hydroxyls may promote the surface reduction-oxidation cycles.

The rGO has excellent electrical conductivity (high electron mobility ($>1000\ cm^2\ V^{-1}\ S^{-1}$). The photoexcited electrons are transferred to rGO and work as the electron carrier to react with adsorbed oxygen molecules on the surface of TiO_2 to form $O_2^{\cdot-}$ Subsequently, the photoexcited holes in the VB can react with H_2O/OH^- and form $^{\cdot}OH$ (hydroxyl radical) species and thus decrease the recombination rate of electron-hole pairs. Since the electron can be transferred onto rGO and trapped by W^{6+}, both surface and bulk recombination of electrons and holes were mitigated by using the W doped TiO_2/rGO composite photocatalyst facilitating enhanced photocatalytic degradation. Therefore, oxidation and reduction processes coexist in the MB dye photodegradation process, accompanied by electrons transfer from the hydroxyls to the $^{\cdot}OH$ radicals and from O_2 to O_2^-, along with the electron-hole pairs with W^{6+}/W^{5+} couples in the catalyst surface. Finally, the principal active species attack the MB dye molecules and undergo reactions to decompose MB into CO_2 and H_2O [71].

4. Conclusions

The tungsten doped TiO_2/rGO composite photocatalyst was successfully fabricated by the PEO with particle addition for efficient MB dye degradation.

- Phase analysis of the prepared photocatalysts confirmed that the W dopant suppressed the rutile formation and reduced the crystal growth of anatase, favouring photocatalytic activity.
- The defects in the crystal lattice increased with the W dopant concentration increase in the coatings. This can favour the light absorption in the visible light spectrum. It also decreased the charge

carriers recombination rate and increased the separation of the photo-induced electrons and holes.

- All the W–TiO_2/rGO composite samples show excellent porous morphologies. The surface area increased with an increase in W dopant concentration, providing more active sites for the degradation of MB dye molecules. Also, the presence of the rGO contributed to a higher specific surface area confirmed by BET analysis.
- The G6W sample with optimum dopant concentration showed a prominent redshift in UV–Vis absorption with a bandgap of 2.88 eV.
- The rGO and W dopant in TiO_2 effectively supressed the electron-hole recombination rate at both surface and lattice level. Also, the hole and hydroxyl radicals were actively participated in the photocatalytic degradation process rather than super oxide radical.
- The highest MB dye degradation efficiency with 93% was achieved on sample G6W with the synergetic effect of visible light absorption by W doping and reduced electron-hole recombination rate by rGO addition.

The present article concludes that the W–TiO_2/rGO composite coating developed by the PEO with particle addition process can be a good candidate for the low-cost, efficient, immobilised and recyclable catalyst for textile wastewater treatment.

Credit author statement

P. Manojkumar: Conceptualization, Methodology, Investigation, Writing – original draft. **E. Lokeshkumar:** Visualization, Writing – review & editing. **C. Premchand:** Writing – review & editing. **A. Saikiran:** Writing – review & editing. **L. Rama Krishna:** Methodology, Writing – review & editing. **N. Rameshbabu:** Conceptualization, Supervision, Funding acquisition, Writing – review & editing.

Declaration of competing interest

The authors declare that they have no known competing financial interests or personal relationships that could have appeared to influence the work reported in this paper.

Acknowledgement

The author (NRB) would also like to thank and acknowledge the financial support from the Science and Engineering Research Board, New Delhi (No. EMR/2016/003259 dated 22-03-2017) to carry out this research.

Appendix A. Supplementary data

Supplementary data to this article can be found online at https://doi.org/10.1016/j.physb.2022.413680.

References

[1] S.S. Muthu, Sustainability in the textile industry, in: S.S. Muthu (Ed.), Textile Science and Clothing Technology, Springer, Heidelberg, 2017, pp. 1–8.
[2] S.C. Bhatia, S. Devraj, Pollution Control in Textile Industry, Milton: WPI, India, 2017.
[3] D.M. Wang, Environmental protection in clothing industry, in: L. Zhu (Ed.), Sustainable Development: Proceedings of the 2015 International Conference on Sustainable Development, World Scientific Publishing Co., Singapore, 2016, pp. 729–735.
[4] L. Bruno, C.Z. Fávaro-Polonio, J.A. Pamphile, J.C. Polonio, Effects of textile dyes on health and the environment and bioremediation potential of living organisms, Biotechnol. Res. Innov. 3 (2019) 275–290.
[5] R. Bhateria, D. Jain, Water quality assessment of lake water: a review, Sustain. Water Resour. Manag. 2 (2016) 161–173.
[6] F.S.A. Khan, N.M. Mubarak, Y.H. Tan, M. Khalid, R.R. Karri, R. Walvekar, E. C. Abdullah, S. Nizamuddin, S.A. Mazari, A comprehensive review on magnetic carbon nanotubes and carbon nanotube-based bucky paper-heavy metal and dyes removal, J. Hazard Mater. 413 (2021) 125375.
[7] X. Li, J.L. Shi, H. Hao, X. Lang, Visible light-induced selective oxidation of alcohols with air by dye-sensitised TiO_2 photocatalysis, Appl. Catal. B Environ. 232 (2018) 260–267.
[8] Y.K. Hashemi, M.T. Yaraki, S. Ghanbari, L.H. Saremi, M.H. Givianrad, Photodegradation of organic water pollutants under visible light using anatase F, N co-doped TiO_2/SiO_2 nano-composite: semi-pilot plant experiment and density functional theory calculations, Chemosphere 275 (2021) 129903.
[9] X. Jiang, Y. Wang, C. Pan, Micro-arc oxidation of TC4 substrates to fabricate TiO_2/YAG: Ce3+ compound films with enhanced photocatalytic activity, J. Alloys Compd. 509 (2011) 137–141.
[10] N.F. Moreira, M.J. Sampaio, A.R. Ribeiro, C.G. Silva, J.L. Faria, A.M. Silva, Metal-free g-C_3N_4 photocatalysis of organic micropollutants in urban wastewater under visible light, Appl. Catal. B Environ. 248 (2019) 184–192.
[11] T. Yildiz, H.C. Yatmaz, K. Öztürk, Anatase TiO_2 powder immobilised on reticulated Al_2O_3 ceramics as a photocatalyst for degradation of RO16 azo dye, Ceram. Int. 46 (2020) 8651–8657.
[12] R. Zouzelka, M. Remzova, J. Plsek, L. Brabec, J. Rathousky, Immobilized rGO/TiO_2 photocatalyst for decontamination of water, Catalysts 9 (2019) 708.
[13] A. Hoseini, B. Yarmand, Immobilization of Fe_2O_3/TiO_2 photocatalyst on the metallic substrate via plasma electrolytic oxidation process: degradation efficiency, J. Nanoparticle Res. 22 (2020) 312.
[14] S. Ebrahimi, A. Bordbar-Khiabani, B. Yarmand, Immobilization of rGO/ZnO hybrid composites on the Zn substrate for enhanced photocatalytic activity and corrosion stability, J. Alloys Compd. 845 (2020) 156219.
[15] V.S. Rudnev, I.V. Lukiyanchuk, M.S. Vasilyeva, V.P. Morozova, V.M. Zelikman, I. G. Tarkhanova, W-containing oxide layers obtained on aluminum and titanium by PEO as catalysts in thiophene oxidation, Appl. Surf. Sci. 422 (2017) 1007–1014.
[16] S. Stojadinovic, N. Radic, N. Tadic, R. Vasilic, B. Grbic, Enhanced ultraviolet light driven photocatalytic activity of ZnO particles incorporated by plasma electrolytic oxidation into Al_2O_3 coatings co-doped with Ce^{3+}, Opt. Mater. 101 (2020) 109768.
[17] E. Lokeshkumar, P. Manojkumar, A. Saikiran, C. Premchand, S. Hariprasad, L. Rama Krishna, N. Rameshbabu, Fabrication of Ca and P containing niobium oxide ceramic coatings on niobium by PEO coupled EPD process, Surf. Coating. Technol. 416 (2021) 127161.
[18] A. Saikiran, S. Hariprasad, P. Manojkumar, L. Rama Krishna, N. Rameshbabu, Effect of laser treatment on morphology and corrosion behaviour of the plasma electrolytic oxidation coatings developed on aluminised steel, Surf. Coating. Technol. 394 (2020) 125888.
[19] A. Hakimizad, K. Raeissi, M.A. Golozar, X. Lu, C. Blawert, M.L. Zheludkevich, Influence of cathodic duty cycle on the properties of tungsten containing Al_2O_3/TiO_2 PEO nano-composite coatings, Surf. Coating. Technol. 340 (2018) 210–221.
[20] P. Manojkumar, E. Lokeshkumar, A. Saikiran, B. Govardhanan, M. Ashok, N. Rameshbabu, Visible light photocatalytic activity of metal (Mo/V/W) doped porous TiO_2 coating fabricated on Cp-Ti by plasma electrolytic oxidation, J. Alloys Compd. 825 (2020) 154092.
[21] G. Yanalak, A. Sarılmaz, G. Karanfil, E. Aslan, F. Ozel, I.H. Patir, Enhanced photocatalytic hydrogen evolution from bandgap tunable Ag2S:X (X=Ni,Co ,Zn , Mn)nanocrystals :Effect of transition metal ions, J. Photochem. Photobiol. Chem. 394 (2020) 112462.
[22] M.S. Vasilyeva, V.S. Rudnev, A.A. Sergeev, K.A. Sergeeva, A.V. Nepomnyaschiy, A. Y. Ustinov, A.A. Zvereva, K.N. Kilin, S.S. Voznesenskiy, Composition, structure, and photocatalytic properties of Fe-containing oxide layers on titanium, Protect. Met. Phys. Chem. Surface 53 (2017) 879–888.
[23] M.S. Vasilyeva, V.S. Rudnev, D.A. Tarabrina, Photocatalytic properties of Zn- and Cd-containing oxide layers on titanium formed by plasma electrolytic oxidation, Prot. Met. Phys. Chem. Surf. 53 (2017) 711–715.
[24] P.S. Basavarajappa, S.B. Patil, N. Ganganagappa, K.R. Reddy, A.V. Raghu, C. V. Reddy, Recent progress in metal-doped TiO_2, non-metal doped/co-doped TiO_2 and TiO_2 nano structured hybrids for enhanced photocatalysis, Int. J. Hydrogen Energy 45 (2020) 7764–7778.
[25] O.Y. Keskin, R. Dalmis, I. Birlik, N.F.A. Azem, Comparison of the effect of non-metal and rare-earth element doping on structural and optical properties of CuO/TiO_2 one-dimensional photonic crystals, J. Alloys Compd. 817 (2020) 153262.
[26] A. Piątkowska, M. Janus, K. Szymański, S. Mozia, C-, N- and S-doped TiO2 photocatalysts: a review, Catalysts 11 (2021) 144.
[27] E.K. Nejman, A.W. Morawski, TiO_2/graphene-based nano-composites for water treatment: a brief overview of charge carrier transfer, antimicrobial and photocatalytic performance, Appl. Catal. B Environ. 253 (2019) 179–186.
[28] M. Yadav, A. Yadav, R. Fernandes, Y. Popat, M. Orlandi, A. Dashora, D.C. Kothari, A. Miotello, B.L. Ahuja, N. Patel, Tungsten-doped TiO2/reduced Graphene Oxide nano-composite photocatalyst for degradation of phenol: a system to reduce surface and bulk electron-hole recombination, J. Environ. Manag. 203 (2017) 364–374.
[29] M. Mohammadi, M.R. Roknabadi, M. Behdani, A. Kompany, Enhancement of visible and UV light photocatalytic activity of rGO-TiO_2 nanocomposites: the effect of TiO_2/Graphene oxide weight ratio, Ceram. Int. 45 (2019) 12625–12634.
[30] S. Ebrahimi, A. Bordbar-Khiabani, B. Yarmand, M.A. Asghari, Improving optoelectrical properties of photoactive anatase TiO_2 coating using rGO incorporation during plasma electrolytic oxidation, Ceram. Int. 45 (2019) 1746–1754.
[31] N. Sun, J. Ma, C. Wang, J. Xue, L. Qiang, J. Tang, A facile and efficient method to directly synthesise TiO_2/rGO with enhanced photocatalytic performance, Superlattice. Microst. 121 (2018) 1–8.
[32] M. Tayebi, M. Kolaei, A. Tayyebi, Z. Masoumi, Z. Belbasi, B.K. Lee, Reduced graphene oxide (RGO) on TiO_2 for an improved photo electrochemical (PEC) and photocatalytic activity, Sol. Energy 190 (2019) 185–194.

[33] M. Aqeel, S. Anjum, M. Imran, M. Ikram, H. Majeed, M. Naz, S. Ali, M.A. Ahmad, TiO_2 @ RGO (reduced graphene oxide) doped nanoparticles demonstrated improved photocatalytic activity, Mater. Res. Express 6 (2019), 086215.
[34] P. Wang, S. Zhan, Y. Xia, S. Ma, Q. Zhou, Y. Li, The fundamental role and mechanism of reduced graphene oxide in rGO/Pt-TiO_2 nano-composite for high-performance photocatalytic water splitting, Appl. Catal. B Environ. 207 (2017) 335–346.
[35] G. Bharath, J. Prakash, K. Rambabu, G. Devanan, Venkatasubbu, A. Kumar, S. Lee, J. Theerthagiri, M.Y. Choid, F. Banat, Synthesis of TiO2/RGO with plasmonic Ag nanoparticles for highly efficient photoelectron catalytic reduction of CO_2 to methanol toward the removal of an organic pollutant from the atmosphere, Environ. Pollut. 281 (2021) 116990.
[36] W. Wang, Z. Wang, J. Liu, Z. Luo, S.L. Suib, P. He, G. Ding, Z. Zhang, Single-step one-pot synthesis of TiO_2 nanosheets doped with sulfur on reduced graphene oxide with enhanced photocatalytic activity, Sci. Rep. 7 (2017) 46610.
[37] X. Zhang, G. Yi, H. Fan, P. Li, Z. Zhang, Y. Wu, L. Chen, C. Zhang, Y. Zhang, Q. Sun, Cobalt doped TiO_2/rGO nanocomposites as highly efficient photocatalyst for water purification, Biomed. J. Sci. Tech. Res. 37 (2020) 29249–29257.
[38] T. Pham, N. Chinh, H. Lee, T. Nguyen-Phan, T.H. Son, C. Kim, E.W. Shin, Cu-doped TiO_2/reduced graphene oxide thin-film photocatalysts: effect of Cu content upon methylene blue removal in water, Ceram. Int. 41 (2015) 11184–11193.
[39] A. Bordbar-Khiabani, S. Ebrahimi, B. Yarmand, Highly corrosion protection properties of plasma electrolytic oxidised titanium using rGO nanosheets, Appl. Surf. Sci. 486 (2019) 153–165.
[40] T. Putta, L. Ming-Chun, J. Anotai, Photocatalytic activity of tungsten-doped TiO_2 with hydrothermal treatment under blue light irradiation, J. Environ. Manag. 92 (2011) 2272–2276.
[41] R.S. Dubey, S. Singh, Investigation of structural and optical properties of pure and chromium doped TiO2 nanoparticles prepared by solvothermal method, Results Phys. 7 (2017) 1283–1288.
[42] D. Komaraiah, E. Radha, J. Sivakumar, MV Ramana Reddy, R. Sayanna, Photoluminescence and photocatalytic activity of spin coated Ag+ doped anatase TiO_2 thin films, Opt. Mater. 108 (2020) 110401.
[43] H. Zhang, J. Cai, Y. Wang, M. Wu, M. Meng, Y. Tian, X. Li, J. Zhang, L. Zheng, Z. Jiang, J. Gong, Insights into the effects of surface/bulk defects on photocatalytic hydrogen evolution over TiO_2 with exposed {001} facets, Appl. Catal. B Environ. 220 (2018) 126–136.
[44] N.D. Sakhnenko, M.V. Ved, A.V. Karakurkchi, Effect of doping metals on the structure of PEO coatings on titanium, Int. J. Chem. Eng. (2018) 4608485.
[45] X. Lu, M. Mohedano, C. Blawert, E. Matykina, R. Arrabal, K.U. Kainer, M. L. Zheludkevich, Plasma electrolytic oxidation coatings with particle additions – a review, Surf. Coating. Technol. 307 (2016) 1165–1182.
[46] A. Amudha, H.D. Shashikala, O.S.A. Rahman, A.K. Keshri, H.S. Nagaraja, Effect of graphene oxide loading on plasma sprayed alumina-graphene oxide composites for improved anticorrosive and hydrophobic surface, Surf. Topogr. Metrol. Prop. (2019) 7024003.
[47] Y. Liu, Y. Shi, S. Zhang, B. Liu, X. Sun, D. Yang, Optimising the interface of C/titania @ reduced graphene oxide nanofibers for improved photocatalytic activity, J. Mater. Sci. 54 (2019) 8907–8918.
[48] R. Long, N.J. English, First-principles calculation of nitrogen-tungsten co-doping effects on the band structure of anatase-titania, Appl. Phys. Lett. 94 (2009) 132102.
[49] A. El Mragui, Y. Logvina, L. Pinto da Silva, O. Zegaoui, J.C.G. Esteves da Silva, Synthesis of Fe- and Co-Doped TiO_2 with improved photocatalytic activity under visible irradiation toward carbamazepine degradation, Materials 12 (2019) 3874.
[50] V. Kumaravel, S. Rhatigan, S. Mathew, M.C. Michel, J. Bartlett, M. Nolan, S. J. Hinder, A. Gascó, C. Ruiz-Palomar, D. Hermosilla, S.C. Pillai, Mo doped TiO_2: impact on oxygen vacancies, anatase phase stability and photocatalytic activity, J Phys. Mater. 3 (2020), 025008.
[51] K.A. Bhabu, A.K. Devi, J. Theerthagiri, J. Madhavan, T. Balu, T.R. Rajasekaran, Tungsten doped titanium dioxide as a photoanode for dye sensitised solar cells, J. Mater. Sci. Mater. Electron. 28 (2017) 3428–3439.
[52] J. Li, J. Xu, W.L. Dai, H. Li, K. Fan, One-pot synthesis of twist-like helix tungsten–nitrogen-co doped titania photocatalysts with highly improved visible light activity in the abatement of phenol, Appl. Catal. B Environ. 82 (2008) 233–243.
[53] S.M. Harshulkhan, K. Janaki, G. Velraj, R.S. Ganapthy, M. Nagarajan, Effect of Ag doping on structural, optical and photocatalytic activity of tungsten oxide (WO_3) nanoparticles, J. Mater. Sci. Mater. Electron. 27 (2016) 4744–4751.
[54] W. Xie, R. Li, Q. Xu, Enhanced photocatalytic activity of Se-doped TiO_2 under visible light irradiation, Sci. Rep. 8 (2018) 8752.
[55] R. Naeem, M.A. Ehsan, A. Rehman, Z.H. Yamani, A.S. Hakeem, M. Mazhar, Single step aerosol assisted chemical vapor deposition of p–n Sn(II) oxide–Ti(IV) oxide nano composite thin film electrodes for investigation of photoelectrochemical properties, New J. Chem. 42 (2018) 5256.
[56] C.H. Kim, B. Kim, K.S. Yang, TiO_2 nanoparticles loaded on graphene/carbon composite nanofibers by electrospinning for increased photocatalysis, Carbon 50 (2012) 2472–2481.
[57] C. Moslah, T. Aguilar, R. Alcántara, M. Ksibi, J. Navas, Synthesis of W-doped TiO_2 by low-temperature hydrolysis: effects of annealing temperature and doping content on the surface microstructure and photocatalytic activity, J. Chin. Chem. Soc. (2018) 1–11.
[58] K. Li, Z. Huang, X. Zeng, B. Huang, S. Gao, J. Lu, Synergetic effect of Ti^{3+} and oxygen doping on enhancing photoelectrochemical and photocatalytic properties of TiO_2/g-C_3N_4 heterojunctions, ACS Appl. Mater. Interfaces 9 (2017) 11577–11586.
[59] G.T.S. How, A. Pandikumar, H.N. Ming, L.H. Ngee, Highly exposed {001} facets of titanium dioxide modified with reduced graphene oxide for dopamine sensing, Sci. Rep. 4 (2014) 5044.
[60] S. Sathasivam, D.S. Bhachu, Y. Lu, N. Chadwick, S.A. Althabaiti, A.O. Alyoubi, S. N. Basahel, C.J. Carmalt, I.P. Parkin, Tungsten doped TiO_2 with enhanced photocatalytic and optoelectrical properties via aerosol assisted chemical vapor deposition, Sci. Rep. 5 (2015) 10952.
[61] F. Ruggieri, D. Di Camillo, L. Maccarone, S. Santucci, L. Lozzi, Electrospun Cu-, W- and Fe-doped TiO_2 nanofibres for photocatalytic degradation of rhodamine 6G, J. Nanoparticle Res. 15 (2013) 1982.
[62] C. Chuaicham, R. Pawar, K. Sasaki, Dye-sensitized photocatalyst of sepiolite for organic dye degradation, Catalyst 9 (2019) 235.
[63] M.A. Rauf, M.A. Meetani, A. Khaleel, A. Ahmed, Photocatalytic degradation of Methylene Blue using a mixed catalyst and product analysis by LC/MS, Chem. Eng. J. 157 (2010) 373–378.
[64] Y.X. Zhang, X.D. Hao, F. Li, Z.P. Diao, Z.Y. Guo, J. Li, pH-Dependent degradation of methylene blue via rational- designed MnO2 nanosheet-decorated diatomites, Ind. Eng. Chem. Res. 53 (2014) 6966–6977.
[65] S. Zhou, Z. Du, X. Li, Y. Zhang, Y.H.Y. Zhang, Degradation of methylene blue by natural manganese oxides: kinetics and transformation products, R. Soc. Open Sci. 6 (2019) 190351.
[66] A.K.M. Atique Ullah, A.K.M. Fazle Kibria, M. Akter, M.N.I. Khan, A.R.M. Tareq, S. H. Firoz, Oxidative degradation of methylene blue using Mn3O4 Nanoparticles, Water Conserv. Sci. Eng. 1 (2017) 249–256.
[67] S.P. Deshmukh, D.P. Kale, S. Kar, S.S.R. hirsath, B.A. Bhanvase, V.K. Saharan, S. H. Sonawane, Ultrasound assisted preparation of rGO/TiO_2 nano-composite for effective photocatalytic degradation of methylene blue under sunlight, Nano-struct. Nano-objects 21 (2020) 100407.
[68] H. Tina, M. Majid, A novel magnetic reusable nano-composite with enhanced photocatalytic activities for dye degradation, Separ. Purif. Technol. 134 (2014) 210–219.
[69] H. Tian, C. Wan, X. Xue, X. Hu, X. Wang, Effective electron transfer pathway of the ternary TiO_2/RGO/Ag nanocomposite with enhanced photocatalytic activity under visible light, Catalyst 7 (2017) 156.
[70] Y. Liu, Y. Shi, X. Liu, H. Li, A facile solvothermal approach of novel Bi_2S_3/TiO_2/RGO composites with excellent visible light degradation activity for methylene blue, Appl. Surf. Sci. 396 (2017) 58–66.
[71] X. Liu, Y. Shi, Y. Dong, H. Li, Y. Xia, H. Wang, A facile solvothermal approach for the synthesis of novel W-doped TiO_2 nanoparticles/reduced graphene oxide composites with enhanced photodegradation performance under visible light irradiation, New J. Chem. 41 (22) (2017) 13382–13390.